Crystallization in the TeO2 - Ta2O5 - Bi2O3 system: from glass to anti-glass to transparent ceramic

Hasnaa Benchorfi, Sébastien Chenu, Jean-René Duclère, Cécile Genevois, Mathieu Allix, Emmanuel Veron, Julie Cornette, Maggy Colas, V.A.G. Rivera, Victor Fuertes, et al.

Crystallization in the TeO_2 - Ta_2O_5 - Bi_2O_3 system: from glass to anti-glass to transparent ceramic

Hasnaa Benchorfi[1,2], Sébastien Chenu[1,3], Jean-René Duclère[1], Cécile Genevois[4], Mathieu Allix[4], Emmanuel Véron[4], Julie Cornette[1], Maggy Colas[1], V.A.G. Rivera[2], Victor Fuertes[2], François Brisset[5], Pierre Carles[1], Samar Aouji[2,6], Philippe Thomas[1], Younès Messaddeq[2], Gaëlle Delaizir[1*]

[1]*Institut de Recherche sur les Céramiques (IRCER), UMR 7315 CNRS, Université de Limoges, Centre Européen de la Céramique, 87068 Limoges, France*

[2]*Centre d'Optique, Photonique et Laser (COPL), Université Laval, Québec G1V 0A6, Canada*

[3]*Institut des Sciences Chimiques de Rennes, Université de Rennes, 35700 Rennes, France*

[4]*Conditions Extrêmes et Matériaux : Haute Température et Irradiation (CEMHTI), UPR 3079 CNRS, 45100 Orléans, France*

[5]*Institut de Chimie Moléculaire et des Matériaux d'Orsay (ICMMO), UMR 8182 CNRS, 91190 Orsay, France*

[6]*Institut de Chimie de la Matière Condensée, Université de Bordeaux, 33608 Bordeaux, France*

*Contact: gaelle.delaizir@unilim.fr

Abstract

Glass samples belonging the TeO_2 - Ta_2O_5 - Bi_2O_3 (TTB) system are prepared by conventional melt-quenching technique and the corresponding vitreous domain is identified. A crystallization study of the 80 TeO_2 - 10 Ta_2O_5 - 10 Bi_2O_3 glass composition versus temperature shows structural transitions from glass to the stabilization of an unreported translucent anti-glass phase and eventually to a fully transparent crystalline ceramic in both the visible and infrared ranges. The structure and microstructure of the anti-glass and ceramic phases are characterized by Powder X-Ray Diffraction, Electron Back-Scatter Diffraction, Transmission Electron Microscopy and Raman spectroscopy. The optical properties of undoped and Er^{3+}-doped transparent samples are also discussed. Up-conversion green emission band shows that the glass intensity is about 2 and 4 times more intense than that of the anti-glass and the ceramic,

respectively. Furthermore, a large spectral bandwidth of 105 nm is found in the anti-glass sample. The advantageous spectroscopic characteristics found here, together with the good thermal stability of these samples, suggest that the anti-glass phase has potential applications as amplification medium for the generation of ultrashort (femtoseconds) pulses.

Keywords:

Glass; Transparent ceramic; telurite; crystallization; Optical properties

1- Introduction

Tellurite glasses exhibit multiple remarkable properties compared to conventional silica-based glasses, notably their low melting point (700-900°C), high refractive index (≈2), high transparency in the infrared region (up to 5−6 μm), interesting non-linear optical properties and high rare earth ions solubility for luminescence [1]–[3]. These properties give tellurite glasses a great deal of interest in various applications such as lasers, fiber optic amplifiers and numerous optical devices including waveguides [2].

Transparent ceramics present several advantages compared to glasses, such as improved mechanical (hardness, tenacity), thermal (thermal conductivity) and optical (luminescence efficiency) properties. However, the elaboration process of ceramics usually requires expensive and complex powder sintering conditions as it remains difficult to completely eliminate the residual pores during their densification which attenuate transparency [4]. The full crystallization of a bulk glass into a transparent ceramic material is a promising alternative to circumvent the disadvantages and technical challenges related to the ceramics obtained by conventional powder sintering processing [5]. However, it is important to ensure that the precise composition of the required crystalline phase is vitrifiable, and to maintain the transparency of the parent glass during the crystallization process. Several ceramics were elaborated via this process, like the barium aluminates $BaAl_4O_7$ [6], strontium aluminates $Sr_3Al_2O_6$ [7],

$Sr_{1+x/2}Al_{2+x}Si_{2-x}O_8$ [8], YAG-Al_2O_3 composite nanoceramics [9] and a tellurite transparent ceramic obtained from the $Bi_{0.8}Nb_{0.8}Te_{2.4}O_8$ glass composition [5], [10].

In this article, we study the synthesis and crystallization of glasses in the TeO_2 - Ta_2O_5 - Bi_2O_3 (TTB) system. In fact, TeO_2 does not easily vitrify by itself. The introduction of modifier and intermediate oxides such as transition metal oxides or alkaline oxides in the glass matrix allows to solve this problem [1]. The addition of alkaline oxides leads to structural depolymerization, which decreases the amplitude of the optical nonlinearity [11], while the addition of transition metal cations (Nb^{5+}, Ta^{5+}) or cations with lone electron pairs (Bi^{3+}, Pb^{2+}) allows maintaining a high optical non-linearity [12], [13].

Several research teams have been interested in the binary systems TeO_2 - Bi_2O_3 [14], [15] and TeO_2 - Nb_2O_5 [14], [16], [17] as well as the ternary system TeO_2 - Nb_2O_5 - Bi_2O_3 (TNB) [15], [16], [18]. The presence of bismuth oxide is noticed in the rare cases of tellurite glasses characterized by a crystallization process occurring in the sample volume. Moreover, the addition of Bi_2O_3 increases the refractive index and lowers the melting temperatures. The TeO_2-Bi_2O_3 system shows a low glass-forming ability and forms glasses at low Bi_2O_3 concentration (up to 5 mol%). The addition of Nb_2O_5, which plays mainly the role of glass-network former in the glasses, to the TeO_2-Bi_2O_3 system significantly improves the glass forming ability [15], [19]. In the TNB system, the specific glass composition $75TeO_2$-$12.5Nb_2O_5$-$12.5Bi_2O_3$ (≡ $Bi_{0.8}Nb_{0.8}Te_{2.4}O_8$) is characterized by a transition from glass to first anti-glass (Fm-3m, a=5.6Å, isostructural with β-$Bi_2Te_4O_{11}$) and then to ceramic (Ia-3, a=11.2Å, isostructural with a $M^{4+}Te_3O_8$ or $A^{3+}_{0.5}B^{5+}_{0.5}Te_3O_8$ structural type when considering the coupled substitution $2M^{4+} \rightleftharpoons A^{3+}+B^{5+}$ [20]) showing a partial ordering of the structure obtained by full and congruent crystallization of the parent glass [10]. An anti-glass is a solid material with a cationic long-range order and a disordered anion sublattice. It can also be described as a “glass of anions” or a disordered crystalline phase. Therefore, the X-ray diffraction pattern of such material shows

sharp peaks while the Raman bands are broad and similar to those of the parent glass. The anti-glass was first studied by Trömel *et al.* in 1983 [21]. Only few anti-glass structures have been reported in the literature such as $SrTe_5O_{11}$, $Ln_2Te_6O_{15}$, $Bi_2Te_4O_{11}$, $Bi_{0.5}Nb_{0.5}Te_3O_8$, $Te_{0.47}Zr_{0.53}O_xF_y$, $Bi_{0.8}Nb_{0.8}Te_{2.4}O_8$ and $In_{2+x}Te_{4-y}O_{11-z}F_{2z}$ [18], [22]–[27].

Niobium and tantalum have many characteristics in common in terms of electronic structure (same column of the periodic table) and they have similar ionic radii (0.64 Å and 0.74 Å, respectively in 6- and 8-fold coordination numbers). Therefore, by analogy with the TNB system, it is expected that some transparent ceramics may be obtained by crystallizing cubic $Bi_xTa_xTe_{4-2x}O_8$ phase from compositions (100-2x)TeO_2-xTa_2O_5-xBi_2O_3 from a full and congruent manner. It is noteworthy that the vitreous domain of this system has already been reported in the literature but no thorough crystallization study has been investigated [28], [29]. In this work, we report that a novel translucent anti-glass phase can be crystallized within the TTB system. Moreover, at higher temperature, a transparent ceramic in both the visible and infrared ranges can be obtained from the parent glass. Finally, the crystallization from amorphous phases is a powerful and non-conventional technique that can lead to the discovery of novel metastable phases with interesting functional properties.

2- Experimental

2.1 Synthesis

Several compositions in the ternary system TeO_2 - Ta_2O_5 - Bi_2O_3 (TTB) were synthesized by the conventional melt-quenching technique in air. High purity precursors (TeO_2 - Todini and Co 99.9%, Ta_2O_5 - Strem Chemicals 99.8%, Bi_2O_3 - Aldrich 99.9%) were weighed in an appropriate amount to get 2g of glass, ground in a mortar-pestle for 5 min, heated in a furnace at 950°C for 30 min in a platinum crucible with intermediate stirring. Then the melt was air-quenched. The vitreous domain was identified in order to determine the optimal compositions

of the TTB system that exhibits i) good thermal stability and ii) a ratio [Bi]=[Ta] (see dashed line in Figure 1) which are likely to give transparent ceramics by the crystallization of cubic $Bi_xTa_xTe_{4-2x}O_8$ phase. The vitreous domain is located on the TeO_2 side with compositions containing relatively similar Ta_2O_5 and Bi_2O_3 contents. Similar results were observed for the TTB vitreous domain previously reported in the literature [29].

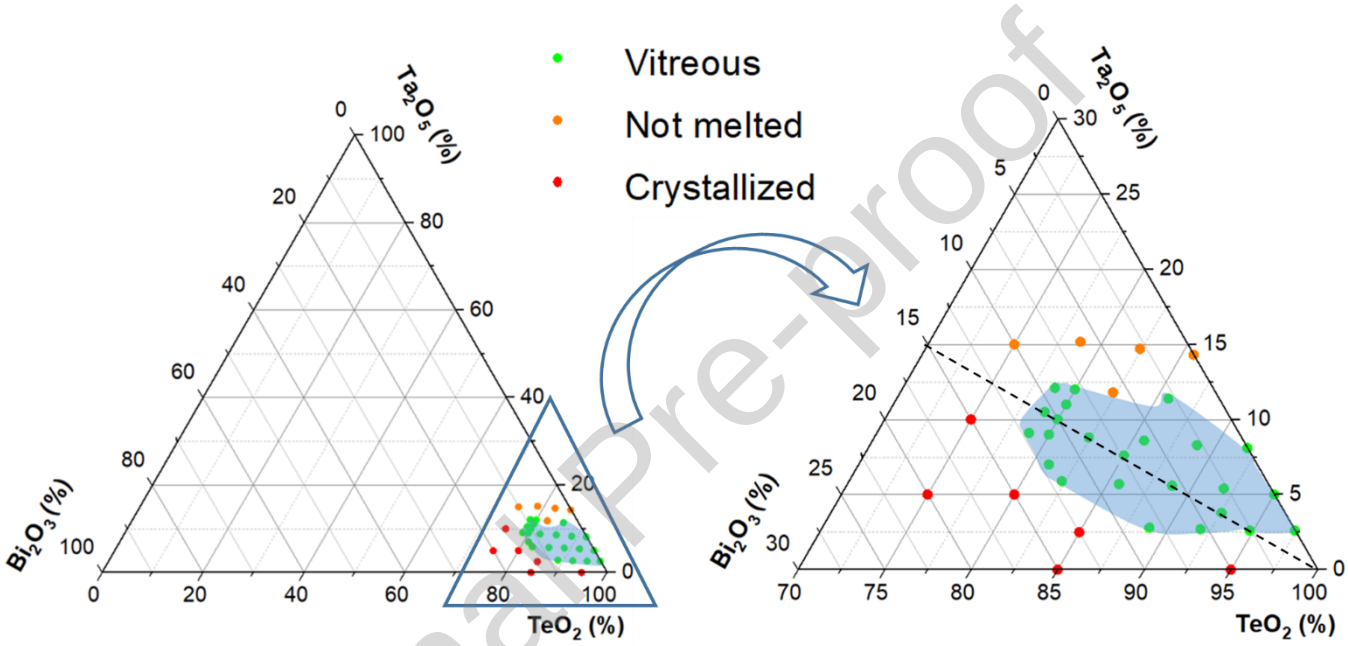

Figure 1.Vitreous domain of the TeO_2-Ta_2O_5-Bi_2O_3 system elaborated at 950°C (the dashed line corresponds to a ratio with [Bi]=[Ta].

2.2 Characterizations

The density of the different bulk samples was determined through the Archimedean principle using a Kern balance. This balance enables weighing solids in air (m_{air}) as well as in a solvent (in our case, ethanol $m_{ethanol}$). If the density of the buoyancy medium is known (ρ_0), the density of the solid (ρ) is calculated as follows:

$$\rho = \frac{m_{air}}{m_{air} - m_{ethanol}} \rho_0$$

Thermal studies were performed on bulk and powdered samples by Differential Scanning Calorimetry (DSC) until 550°C on a TA instrument AQ20 equipment at a heating rate of 10°C/min.

Powder X-Ray Diffraction (PXRD) data were collected using a D8 Advance Bruker laboratory diffractometer (CuKα radiation) equipped with a LynxEye XE detector. Room temperature diffraction patterns were collected from 10 to 80° (2θ) with a 0.012° step size and an acquisition time of 5 s/step. Variable temperature (VT-PXRD) data were collected under air using an XRK900 Anton Paar furnace. The powder sample was placed into a corundum sample holder. Data were collected from 10 to 80° (2θ) with a 0.024° step size and an acquisition time of 1 s/step. Structure refinements were performed from powder diffraction data using the Fullprof academic software which enables the use of the anisotropic broadening function [30].

Raman spectra were recorded using an In Via Reflex Renishaw micro-Raman spectrometer at 532 nm. A grating of 2400 gr/mm was used, along with an objective x100 while using a laser power of 3 mW at the sample to avoid any damage of the sample.

Electron backscatter diffraction (EBSD) maps were recorded on both anti-glass and ceramic materials using an OIM^{TM} TSL/EDAX system mounted on a FEG-SEM (Zeiss SUPRA 55 VP) microscope in order to confirm the crystalline nature of the samples and to visualize the microstructure, grain size as well as the crystal orientation using OIM 8. The data were acquired at a high voltage of 20 kV in in VP mode. The pixels whose confidence index is under 0.1 were removed from the maps.

The nanostructure of the samples was characterized by Transmission Electron Microscopy (TEM) micrographs, Scanning Transmission Electron Microscopy – High Angle Annular Dark Field (STEM-HAADF) imaging and EDS elemental analyses. These experiments were performed on a JEOL ARM 200F (JEOL Ltd.) Cold FEG TEM operating at 80 kV, equipped with a double spherical aberration corrector and fitted with a JEOL SDD CENTURIO EDS

system. STEM-HAADF imaging and STEM-EDS elemental maps were acquired with a 0.1 nm probe size. The samples were prepared prior to (S)TEM observations by Focused Ion Beam system (FIB, Zeiss Crossbeam 550).

The refractive indices were recorded by a Metricon Model 2010 Prism Coupler using four different wavelengths at 632.8, 972.4, 1308.2 and 1537.7 nm.

Optical transmission measurements were carried out in the UltraViolet (UV) – visible – Near-InfraRed (NIR) range (200 – 2500 nm) using a Varian Cary 5000 spectrophotometer.

NIR and upconversion (UC) luminescence spectra were obtained by pumping the samples at 980 nm with a 400 mW laser diode. The signal was collected on a Horiba Nanolog spectrometer coupled with an InGaAs cooled detector or an R2658 photomultiplier (PMT). In the emission measurements, the luminescence signal is detected in a reflective geometry. Here the sample angle and laser beam are the same for all, and the spot laser is 3 mm. All these conditions guarantee that the excited volume is the same.

For the lifetime decay measurements, an OPO was used as the pump source and an Edinburgh FLS1000 spectrometer coupled with a Tektronix oscilloscope was employed to record the time-dependent decays.

3- Results and discussion

3.1 Thermal properties and chemical compositions

DSC experiments were performed on bulk and powdered glass samples in order to determine the glass transition (T_g) and crystallization temperature (T_c) of the different compositions illustrated in Figure 1. Table 1 gathered the T_g and temperature of first crystallization, T_{c1} as well as the Dietzel criterion (T_{c1}-T_g) for some vitreous compositions.

Table 1: T_g, T_{c1} and Dietzel criterion (T_{c1}-T_g) for some glass compositions in the TeO_2-Ta_2O_5-Bi_2O_3 vitreous domain.

Glass composition	T_g (± 1°C)	T_x (± 1°C)	T_{c1}-T_g
79 TeO_2 – 10.5 Ta_2O_5 – 10.5 Bi_2O_3	389	473	84
80 TeO_2 – 8 Ta_2O_5 – 12 Bi_2O_3	370	420	50
80 TeO_2 – 10 Ta_2O_5 – 10 Bi_2O_3	380	487	107
81 TeO_2 – 7 Ta_2O_5 – 12 Bi_2O_3	368	406	38
82 TeO_2 – 9 Ta_2O_5 – 9 Bi_2O_3	380	515	135
88 TeO_2 – 6 Ta_2O_5 – 6 Bi_2O_3	346	420	74
89 TeO_2 – 8 Ta_2O_5 – 3 Bi_2O_3	367	503	136
92 TeO_2 – 3 Ta_2O_5 – 5 Bi_2O_3	326	371	45
92 TeO_2 – 5 Ta_2O_5 – 3 Bi_2O_3	343	467	124
95 TeO_2 – 2.5 Ta_2O_5 – 2.5 Bi_2O_3	323	377	54
92 TeO_2 – 8 Ta_2O_5	360	496	136
95 TeO_2 – 5 Ta_2O_5	330	451	121
97.5 TeO_2 – 2.5 Ta_2O_5	319	386	67

T_g increases when increasing the Ta_2O_5 concentration due to the higher Ta-O energy bond (839 kJ/mol) compared to Bi-O (337 kJ/mol) and Te-O (391 kJ/mol).

First attempts were made on the 80TeO_2-10Ta_2O_5-10Bi_2O_3 (80TTB) glass composition. It is noteworthy that the choice of compositions with a ratio [Bi]=[Ta] is limited since compositions with higher content in TeO_2 lead to the crystallization of unwanted TeO_2 crystalline phase and compositions with lower TeO_2 content are thermally unstable (boundary of the vitreous domain). The 80TeO_2-10Ta_2O_5-10Bi_2O_3 bulk sample exhibits a glass transition temperature T_g of 380°C and temperatures of first and second crystallization T_{c1} and T_{c2} of 487°C and 531°C respectively (Figure 2). The powdered and bulk thermograms, especially the first crystallization peak, do not superimpose while the second peak is perfectly superimposable. Previous studies on the 75TeO_2-12.5Nb_2O_5-12.5Bi_2O_3 (75TNB) composition showed that these two similar peaks correspond to the glass → anti-glass and to the anti-glass → ceramic transformations [10], [18]. The second crystallization peak is therefore rather a phase transition than a crystallization. The nominal composition of the 80TTB glass was checked by SEM-EDS and the results confirmed the absence of evaporation and deviation in glass composition.

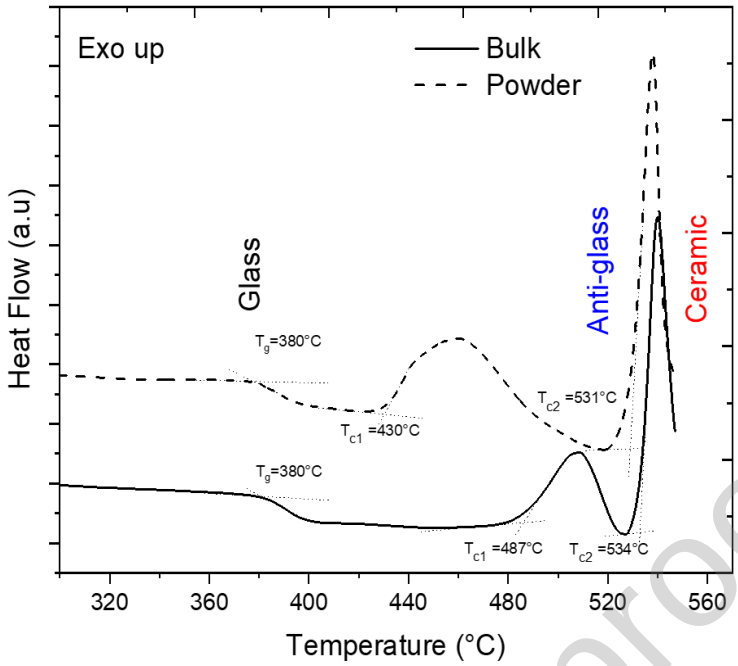

Figure 2. DSC thermograms of the 80 TeO_2 - 10 Ta_2O_5 -10 Bi_2O_3 parent glass on bulk and powdered samples (heating rate: 10°C/min).

The glass bulk was thus synthesized as described above except that the mixture was poured on a brass plate previously heated at T_g - 50°C in order to prevent glass cracking. Then, an annealing treatment was performed at T_g - 10°C for 1h before cooling to room temperature in order to release the mechanical stresses in the glass resulting from the thermal quenching.

3.2 Structure of samples

Based on DSC measurements, VT-PXRD experiments were performed on the 80TTB glass powder composition from RT to 600°C (Figure 3a). Crystallization starts at 400°C (powder sample) and extra peaks arise at 500°C. By analogy with the TNB system, the first crystalline phase appearing may correspond to a disordered anti-glass phase which corresponds to a topological ordering (long range) of the cations in the structure while the extra peaks appearing at higher temperature may correspond to a more ordered structure that exhibits some chemical ordering of the cationic and anionic positions.

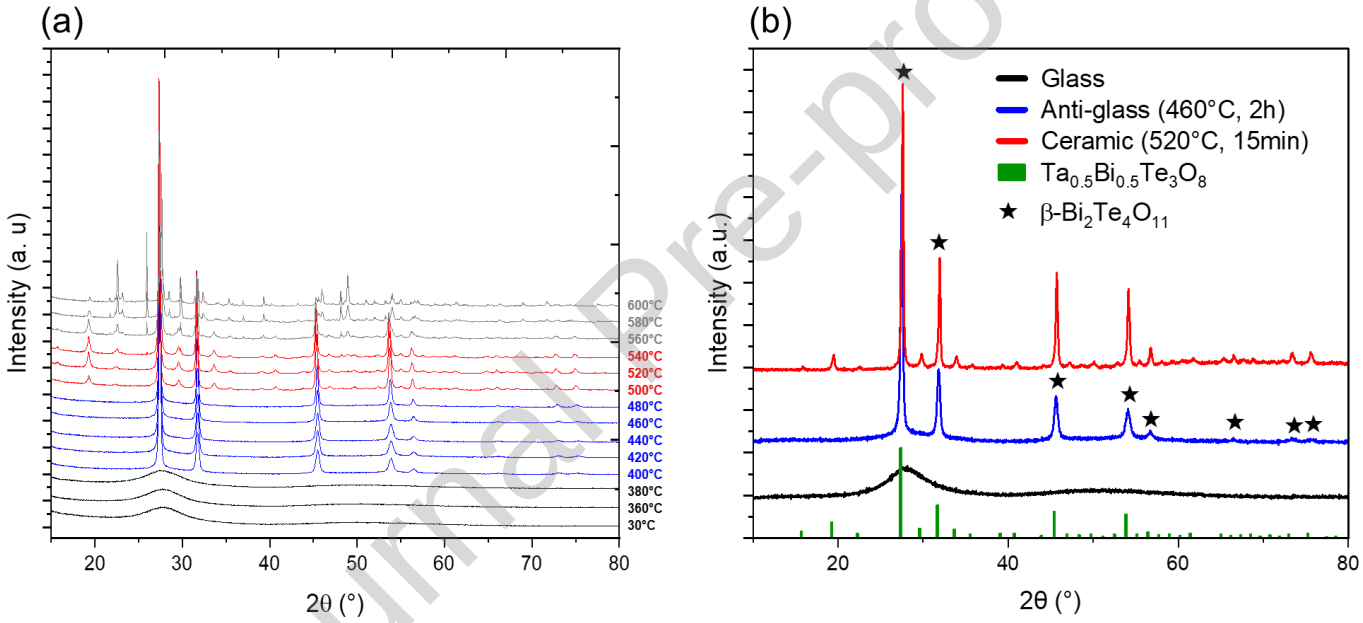

Figure 3. (a) VT-PXRD experiments performed on the 80TeO$_2$-10Ta$_2$O$_5$-10Bi$_2$O$_3$ glass powder, (b) Powder X-ray Diffraction of the parent glass, the anti-glass and the ceramic (green ticks correspond to the Ta$_{0.5}$Bi$_{0.5}$Te$_3$O$_8$ phase (JCPDS 005-8268) and stars ★ to the β-Bi$_2$Te$_4$O$_{11}$ (JCPDS 052-0055))

From DSC and HTXRD results, several crystallization heat treatments were performed on both glass compositions to isolate the anti-glass and crystalline phases:

- At 460°C and 470°C (close to the temperature of the first crystallization peak on bulk sample) for durations ranging from 30 min to 5 h.

- At a temperature of 520°C and 530°C (close to the temperature of the second crystallization peak on bulk sample) for durations ranging from 15 to 60 minutes.

Experimentally, the best results in terms of transparency were obtained for a heat-treatment of 460°C for 2h and 520°C for 15 minutes to get the anti-glass and ceramic materials respectively. The amorphous or crystalline nature of the different samples was determined by X-ray powder diffraction (Figure 3b).

The crystalline phase present after a heat treatment at 460°C for 2h can be indexed with the cubic anti-glass phase β-$Bi_2Te_4O_{11}$ (JCPDS 052-0055) [24]. Regarding the heat treatment at higher temperature (520°C), additional peaks appear. The crystalline phase can then be indexed with $Ta_{0.5}Bi_{0.5}Te_3O_8$ (JCPDS 005-8268) [20] (Figure 3b).

To go further in the structural understanding of these materials, Raman experiments were performed on the 80TTB glass, anti-glass (460°C, 2h) and ceramic (520°C, 15 min) samples. The Raman bands of the sample crystallized at 460°C for 2h are as broad as those of the parent glass while Bragg peaks are visible by XRD measurements of the same samples (Figure 4a). These experimental observations reflect the existence of both high local structural disorder as shown by Raman and long-range cationic order as testified by the presence of diffraction peaks in XRD, which is in good agreement with the "anti-glass" nature of this intermediate phase [31]. The transition from translucent anti-glass to transparent ceramic with the increase of the heat treatment temperature leads to the narrowing of Raman bands typical of an ordered crystalline compound. It is noteworthy that this transition was already evidenced in the case of the TNB composition [10]. The Raman spectra of both the glass and anti-glass materials are similar and can be decomposed with six Gaussian functions (Figure 4b). Raman peak positions, and their corresponding attributions, are gathered in Table 2 [32], [33]. For example, in the glass and anti-glass samples, the band at around 450 cm^{-1} can be assigned to symmetric stretching vibrations of Te-O-Te bridges. The band at 650 cm^{-1} is related to the symmetric

stretching of Te-O in both TeO_4 and TeO_3 units. The band at 740 cm^{-1} and 780 cm^{-1} are attributed to the stretching vibrations of Te-O in TeO_3 and TeO_{3+1} units with non-bridging oxygens [32]. In the ceramic sample, the attribution is more complex as a classical interpretation is not possible in view of the description of the ceramic cubic structure determined from the Rietveld refinement as shown later. The presence of extra bands at 281 cm^{-1} and 875 cm^{-1} in the ceramic are attributed to the stretching of heavy atoms (Bi, Te and Ta) and stretching of Ta/Bi-O bonds respectively.

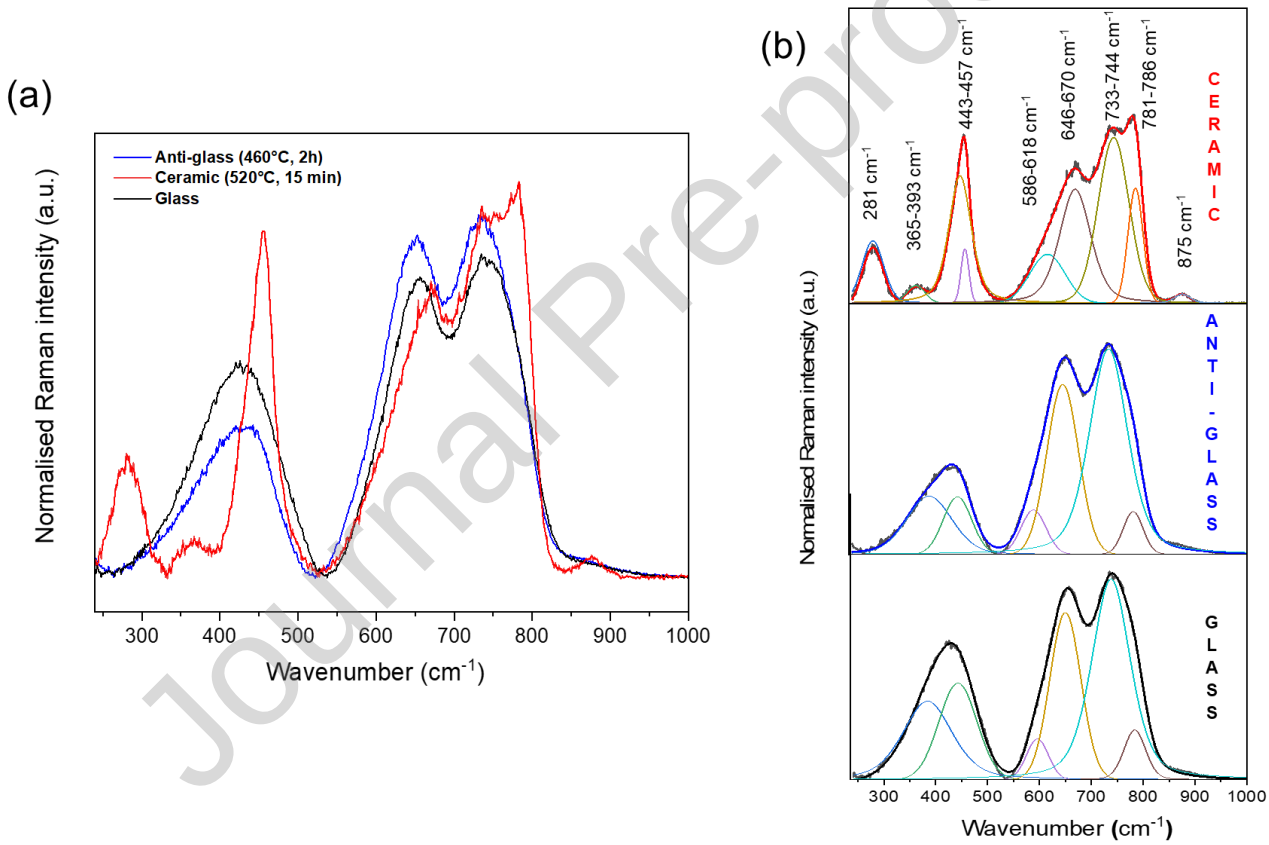

Figure 4. (a) Normalized and baseline subtracted Raman spectra of the parent glass, its corresponding anti-glass (460°C, 2h) and ceramic (520°C, 15 min). (b) Decomposition of 80TTB (glass, anti-glass, ceramic) Raman spectra.

Table 2. Assignment of Raman bands in TTB samples.

Wavenumber (cm^{-1})	**Attributions (glass and anti-glass)**	**Attributions (ceramic)**
281		Stretching of heavy atoms
365-390-392-393	Bending of symmetric Te-O-Te bridges	Bending of symmetric O-Ta/Bi1-O and Te-O-Te bridges
443-444-446-457	Bending of asymmetric Te-O-Te bridges	Bending of asymmetric O-Ta/Bi1-O and Te-O-Te bridges
586-592-595-618	Asymmetric bending of TeO_4 polyhedra	
646-649-651-670	Symmetric bending of TeO_4 polyhedra	Stretching of Ta/Bi-O bonds of Ta/BiO_6 octahedra
733-734-737-744	Stretching of non-bonding Te-O of TeO_3 polyhedra	
781-784-784-786	Stretching of non-bonding Te-O of TeO_4 polyhedra	
875		Stretching of Ta/Bi-O bonds

As stated above, the XRD pattern of the anti-glass phase matches well the β-$Bi_2Te_4O_{11}$ (JCPDS 052-0055) indexation (a = 5.61 Å, Fm-3m). Given the large amount of disorder in this structure (unique 4a (0, 0, 0) mixed cationic site and strong positional disorder in the anionic network), Rietveld refinement was not conducted. The structure is however isostructural with β-$Bi_2Te_4O_{11}$ [24] and the $Bi_{0.8}Nb_{0.8}Te_{2.4}O_8$ anti-glass phases [10].

The XRD pattern of the ceramic phase exhibits extra reflections compared to the anti-glass phase, as already observed for the $Bi_{0.8}Nb_{0.8}Te_{2.4}O_8$ composition [10]. A similar structural ordering seems to occur while transiting from the anti-glass phase to the ceramic, as the 80TTB ceramic matches well the AB_3O_8-type structure indexation ($TiTe_3O_8$ prototype phase, Ia-3 space group, a = 11.2Å), a superstructure of the fluorite structure. Therefore, the extra-reflections observed for the ceramic phase are superstructure reflections mainly coming from the ordering of the cations and anions, initially randomly distributed. In order to gain more insight into the TTB ceramic structure, a Rietveld refinement was initiated using the $Bi_{0.8}Nb_{0.8}Te_{2.4}O_8$, i.e. $(Bi_{0.2}Nb_{0.8})(Bi_{0.6}Te_{2.4})O_8$, ceramic structure as a starting model (2 cationic sites (8a 0, 0, 0 for A and 24d x, 0, 1=4 for B) and 2 oxygen sites (48e x,y,z and 16c x, x, x).

The A site lies in an almost perfectly symmetric octahedral environment whereas the B site is located slightly off the plan formed by its 4 oxygen neighbors. Since the Bi^{3+}, Ta^{5+} and Te^{4+} cations can a priori occupy both A and B sites, it is not possible to determine the compositions of the cationic sites from free refinement of powder diffraction data only. Therefore, as for the $Bi_{0.8}Nb_{0.8}Te_{2.4}O_8$ ceramic, we chose to consider that Ta^{5+} is exclusively located on the octahedral A site (8a cationic site). This is a reasonable assumption as in the literature Ta would rather sit in an octahedral environment whereas both Bi and Te, with their electronic lone pair, can occupy invariably a much distorted site or an octahedral site [20]. Moreover, the AB_3O_8 structure can only be accessed if the Ta content is equal to the Bi content (electroneutrality) therefore we used this condition, considering a $(Bi_{0.5-x-y}Ta_{0.5+x}Te_y)(Bi_{2x+y}Te_{3-2x-y})O_8$ general formulae, in our Rietveld refinements. Our first attempts showed a reasonably good fit while considering anisotropic line broadening. Indeed, as for the TNB ceramic, the superstructure reflections clearly appeared much broader than the intense ones (fundamental reflections) previously observed for the anti-glass material. The reason of this observation may lie in the ordering that is only carried out on small domains of coherence as it will be shown with TEM experiments (see section 3.3). The refinement of the x value was rather unstable, which is not surprising given the lack of information (few peaks linked to the small cell and high symmetry), the correlation of the cationic site compositions with the atomic displacement parameters and the poor contribution of oxygen in PXRD which is here used to scale the fit. In the final model, we then chose to fix the x value to the composition determined by STEM-EDS on several crystallites (x=0.125) as mentioned in section 3.3. No Te seems to be present on the A site (y=0). We therefore obtained the $(Bi_{0.375}Ta_{0.625})(Bi_{0.25}Te_{2.75})O_8 \equiv Bi_{0.625}Ta_{0.625}Te_{2.75}O_8$ formula. The resulting Rietveld plot of PXRD data is shown in Figure 5.

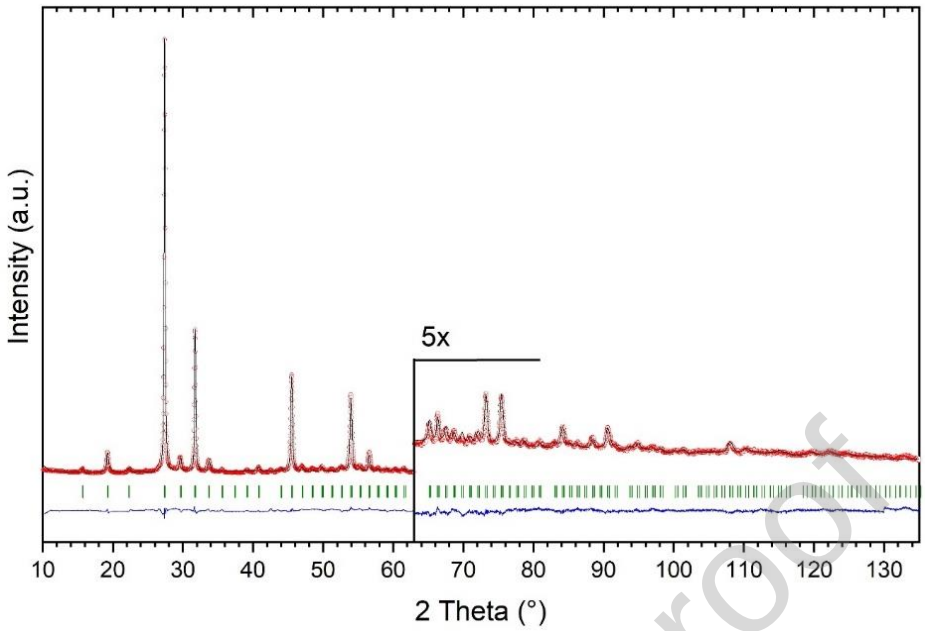

Figure 5. Experimental (red circles), fitted (black solid line) and difference curve (blue solid line) of the XRD Rietveld diagram refinement of the $Bi_{0.625}Ta_{0.625}Te_{2.75}O_8$ ceramic material. Reliability factors are RB = 10.7%, RF = 10.9%, x2 = 13.

The final refined structural parameters and interatomic distances of the $Bi_{0.625}Ta_{0.625}Te_{2.75}O_8$ ceramic are listed in Tables 3 and 4, while a view of the average structure is presented in Figure 6.

Table 3. Atomic coordinates and occupancies determined for the $Bi_{0.625}Ta_{0.625}Te_{2.75}O_8$ ceramic phase from Rietveld refinement of X-ray powder diffraction data recorded at room temperature.[a]

Atom	Site	X	Y	Z	Occupancy	Uiso (A^2)
Bi1	8a	0	0	0	0.375[b]	0.019(1)
Ta1	8a	0	0	0	0.625[b]	0.019(1)
Te2	24d	0.2234(2)	0	0.25	0.917	0.043(3)[b]
Bi2	24d	0.2234(2)	0	0.25	0.083	0.043(3)
O1	48e	0.4298(1)	0.1282(1)	0.4067(1)	1	0.012[c]
O2	16c	0.1830(1)	0.1830(1)	0.1830(1)	1	0.012[c]

a : Space group Ia-3, a = 11.2649(2)Å.

b: No Te1 on A site
c : Fixed parameter.

Table 4. Bond lengths for the $Bi_{0.625}Ta_{0.625}Te_{2.75}O_8$ ceramic phase from Rietveld refinement of X-ray powder diffraction pattern collected at room temperature.

Bond	**Length (Å)**
Ta1/Bi1/Te1 – O1 (x6)	1.953(3)
Bi2/Te2 – O1 (x2)	2.158(3)
Bi2/Te2 – O2 (x2)	2.242(2)

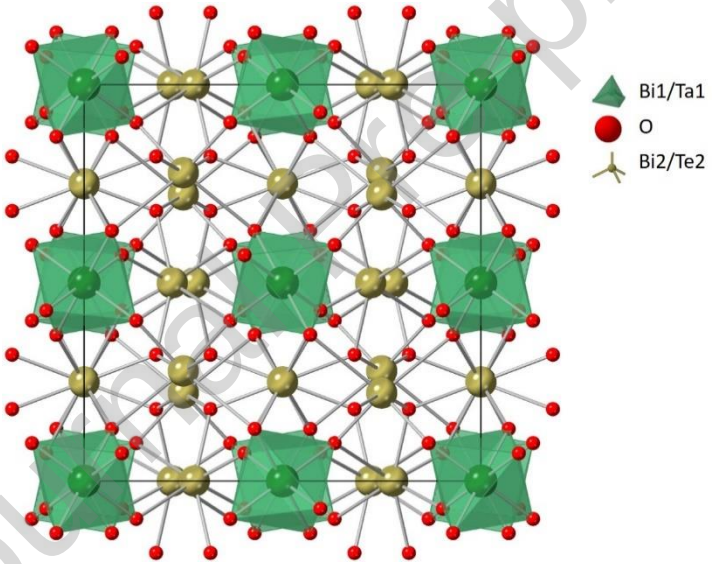

Figure 6. Schematic view along the [001] direction of the $Bi_{0.625}Ta_{0.625}Te_{2.75}O_8$ ceramic structure.

3.3 Microstructure of samples

The EBSD observations on the 80TTB anti-glass (460°C, 2h) and ceramic (520°C, 15 min) samples show that both materials are fully crystallized at the microscopic scale with no preferential orientation as depicted by the pole figures and no residual glass is detectable at the grain boundaries (Figures 7a and 7b). We can also observe an increase of the size of the crystalline domains from the anti-glass (~ 340 nm) to the ceramic (~ 680 nm) (Figures 7c and

7d). This result is consistent since the ceramic is heat treated at a higher temperature than the anti-glass.

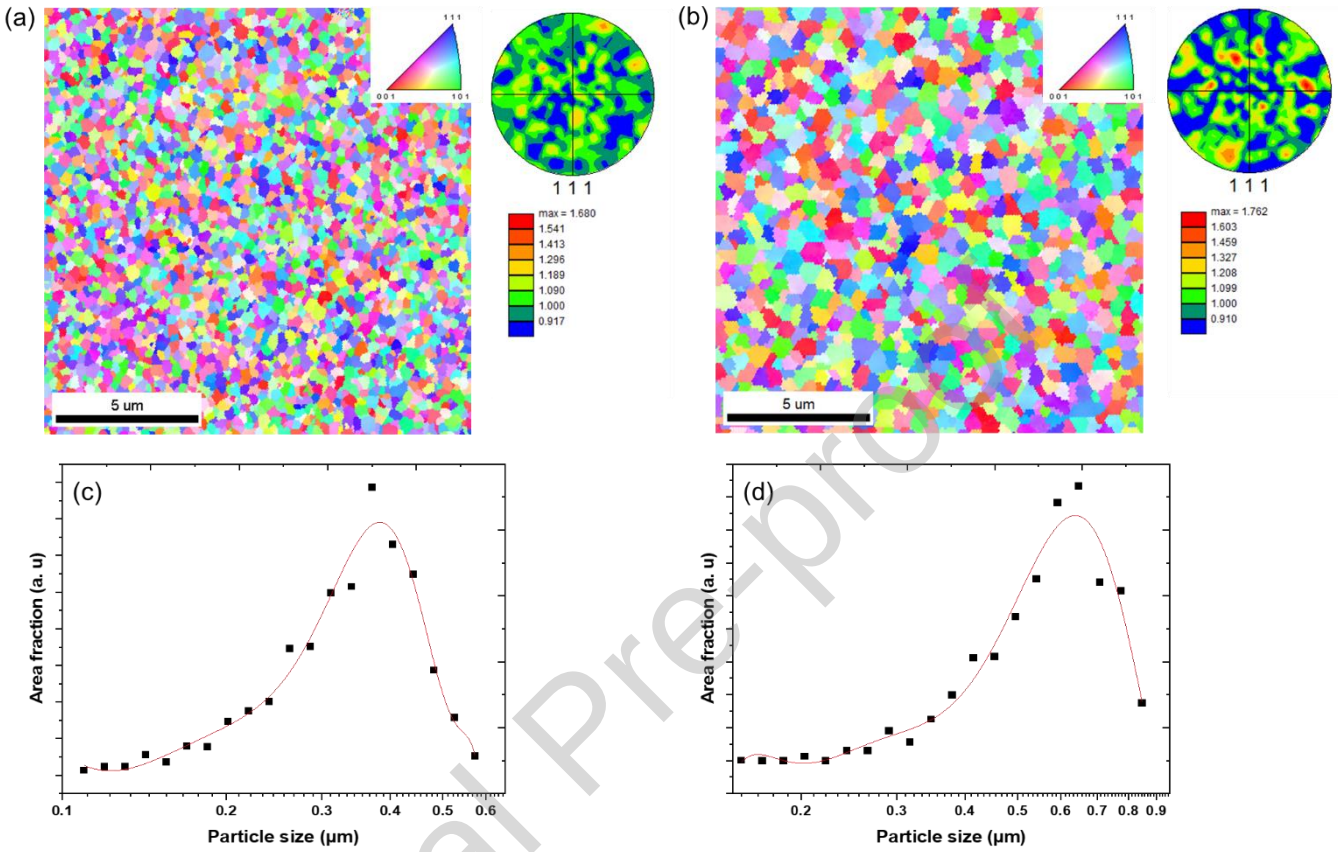

Figure 7. EBSD maps of the (a) anti-glass and (b) the ceramic with the Inverse Pole Figure (IPF) legend and pole figures. Particle size distribution determined from EBSD map (c) anti-glass, (d) ceramic. The red curve serves as a guide for the eyes.

To gain deeper understanding of the 80TTB samples, SEM and TEM observations were performed on both the anti-glass and the ceramic samples. TEM images of the anti-glass (460°C, 2h) FIB lamella is presented in Figure 8. The sample exhibits some large domains of few hundreds of nm with preferential crystalline orientation that can be indexed with the structure of the cubic $Bi_{0.8}Nb_{0.8}Te_{2.4}O_8$ anti-glass phase (Fm-3m a=5.61Å) [10]. The size of these domains (few hundreds of nm) is consistent with the EBSD images recorded on the same sample (Figure 7a). The SAED pattern (inset of Figure 8a) matches perfectly the previously reported TNB anti-glass phase [10]. Each domain is constituted of smaller grains (~ 50 nm) as

depicted in Figure 8b, giving rise to complex multi-scale microstructure of such material. High resolution transmission electron microscope (HRTEM) image shows the existence of an intermediate nanostructure between amorphous and crystalline areas as depicted by the FFT image (inset of Figure 8c). Indeed, we can observe both bright spots and diffuse rings showing the partial ordering of the anti-glass formation and the presence of residual glass respectively. High-angle annular dark-field scanning transmission electron microscopy (STEM-HAADF) reveals a tenuous contrast (presence of slightly darker veins) that likely results from a density contrast (presence of residual glass) combined with a chemical composition contrast (Figure 8d). Unfortunately, it was not possible to get the chemical composition of the veins as the sample deteriorates under the electron beam (Te and Bi volatilization).

The composition of the anti-glass phase has been measured by STEM-EDS and is found to be $82.9TeO_2$-$8.55Ta_2O_5$-$8.55Bi_2O_3$ (mol %).

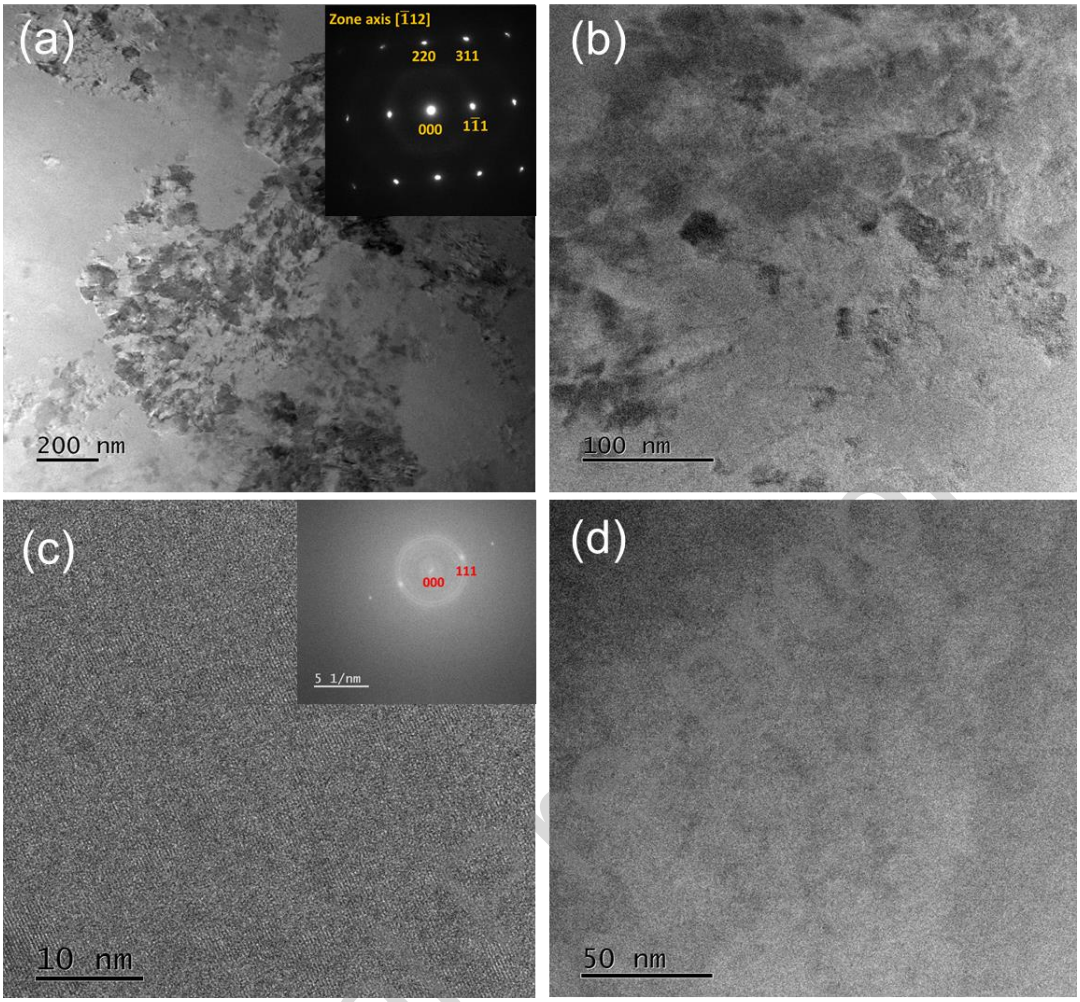

Figure 8. (a,b) Bright Field TEM micrograph of the 80 TTB anti-glass (400°C 2h) (insert of (a): Selected Area Electron Diffraction pattern along the [$\bar{1}$12] zone axis), (c) HRTEM image with in insert associated Fast Fourier Transform (FFT), (d) STEM-HAADF image revealing local density variations.

The microstructure of the 80TTB ceramic sample was also investigated. SEM-EDS elemental maps reveal that the sample is rather homogeneous at the microscopic scale which is in favor of a congruent crystallization mechanism (Figure 9a). Bright Field TEM micrographs of the FIB lamella prepared from a transparent ceramic (Figure 9b) shows grains with sizes ranging from 30 nm to 120 nm. From EBSD observations, the crystalline domains are in fact made of several nanocrystals showing, like in the case of the anti-glass phase, a complex multi-scale microstructure (see red arrows in Figure 9c). SAED patterns exhibit sharp diffraction spots with the absence of an amorphous ring which demonstrates local structural ordering (Figure 9c).

STEM-EDS reveals that the chemical composition of the grains is about 81.4TeO_2-9.3Ta_2O_5-9.3Bi_2O_3 which is consistent with the presence of the $Bi_{0.625}Ta_{0.625}Te_{2.75}O_8$ cubic phase and which is close to the nominal composition 80TTB (≡ $Bi_{0.67}Ta_{0.67}Te_{2.67}O_8$).

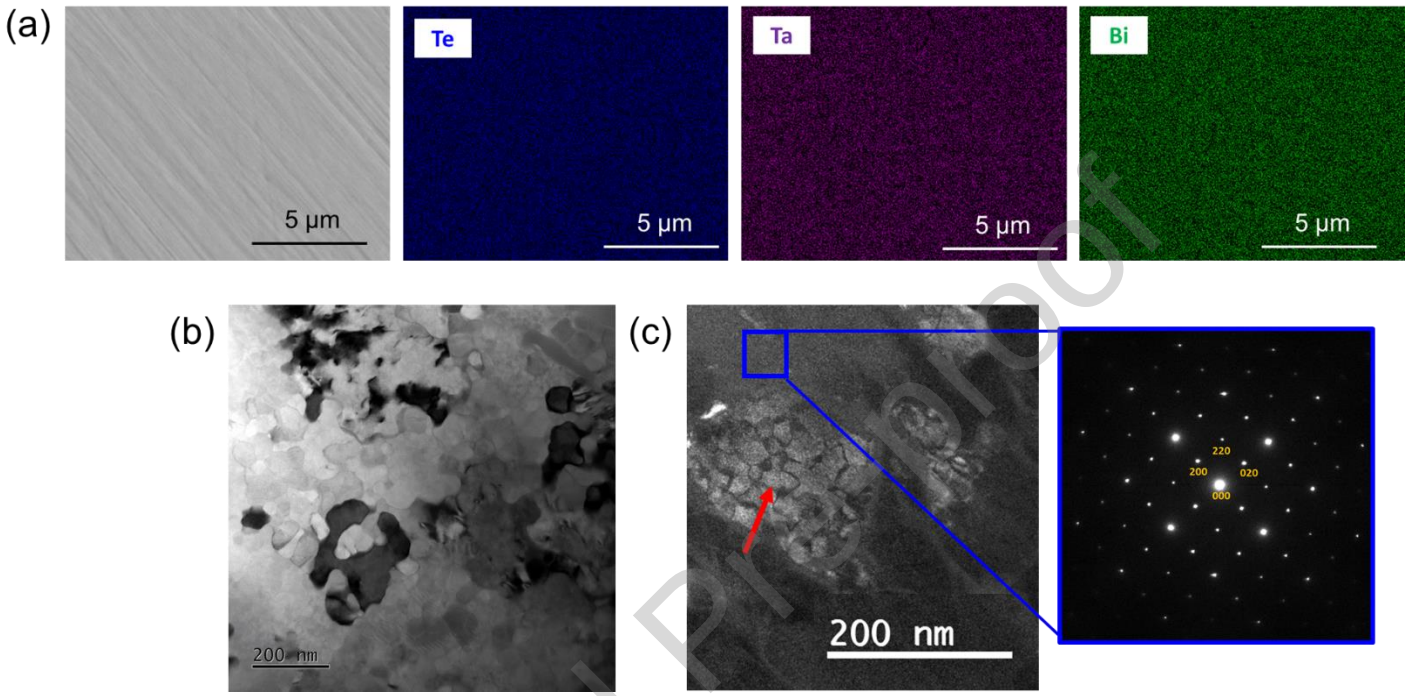

Figure 9. 80TeO_2-10Ta_2O_5-10Bi_2O_3 ceramic (a) SEM-EDS elemental mapping (b) Bright Field TEM micrograph of the microstructure and (c) Dark field TEM image with the corresponding SAED pattern, oriented along the [001] zone axis, of crystalline zone.

Finally, the crystallization mechanism at play for the 80TeO_2-10Ta_2O_5-10Bi_2O_3 is similar from the one observed in the TNB system where the ratio of the nominal composition [Bi]=[Nb] allows the full and congruent crystallization of the parent glass.

3.4 Optical properties

Tellurite glasses doped with rare-earth ions are permanently under research due to diverse technological applications. Indeed, the Er^{3+}-doped tellurite glasses play an important role in telecom due to their broadband and high-intensity emission centered at 1.54 µm [34]. Therefore, in this study, as a supplement to the undoped samples, we prepared samples 80TeO_2-10Ta_2O_5-

$10Bi_2O_3$ with 0.5% Er^{3+} ions (mol %) in addition to study the optical properties of our glass, anti-glass and ceramic, and their possible applications in optical telecommunications (Er_2O_3 was added to the initial composition, 99.995% Strem Chemicals).

The transmittance of the undoped samples is displayed in Figure 10a. The transmission of the parent glass reaches a maximum of 76.4% in the visible and near infrared region. For the anti-glass and the ceramic, the transmission is maximum in the near infrared range then gradually decreases in the visible range, especially for the anti-glass. Measured average refractive index values (n) for the glass, anti-glass and ceramic are n = 2.132(5), n= 2.179(7) and n=2.181(7) respectively at λ = 1537.7 nm (Figure 10e). This corresponds to a 77% for the glass and 77.5% for the anti-glass and ceramic maximum theoretical transmittance value (the residual theoretical loss is a consequence of Fresnel reflections losses at the sample air/interfaces). Transparency in the glass sample is therefore found to match the theoretical value indicating an absence of scattering centers within the amorphous sample. The ceramic displays outstanding transparency over a wide range of wavelengths from the IR well into the visible range while the transmittance of the anti-glass is only high in the infrared range. In both samples, the scattering losses clearly depend on the wavelength and increases from the IR down to the UV range. The multiphonon cut-off wavelength is around 6.5 µm for all the samples (see inset of Figure 10a). Visually, the anti-glass sample is translucent in the visible range while the ceramic is transparent (Figure 10b). This observation can be related to the microstructure of the anti-glass and ceramic samples (see Figures 8 and 9). Indeed, in the anti-glass, some chemical inhomogeneities as well as some residual glass with a different refractive index may induce some birefringence and as a consequence, some light scattering effects. These light scattering effects are less pronounced in the ceramic which exhibits a higher transmittance in the visible range than the anti-glass, as testified by the visual aspect (Figure 10b).

Figure 10d shows the absorption bands attributed to the electronic transitions from the ground state of the Er^{3+} ions to the excited states, i.e., $^4I_{15/2} \rightarrow \{^4F_{3/2}$, $^4F_{5/2}$, $^4F_{7/2}$, $^2H_{11/2}$, $^4S_{3/2}$, $^4F_{9/2}$, $^4I_{9/2}$, $^4I_{11/2}$ and $^4I_{13/2}\}$ which correspond to the wavelengths 445, 450, 488, 522, 545, 653, 794, 976 and 1535 nm, respectively. Such absorption bands are identified in all the samples, where the peak position for each transition is almost the same (± 2 nm). Furthermore, the structural change observed in the undoped samples are maintained in the Er^{3+}-doped glass and ceramic samples while we observe in this case that visually, both the anti-glass and ceramic behave similarly and look translucent due to scattering effect (residual glass, inhomogeneities) (Figure 10c). In addition, one can see that the Er^{3+}-doped tellurite anti-glass shows a very comparable absorption/scattering tail to the Er^{3+}-doped ceramic within the visible and NIR ranges (Figure 10d).

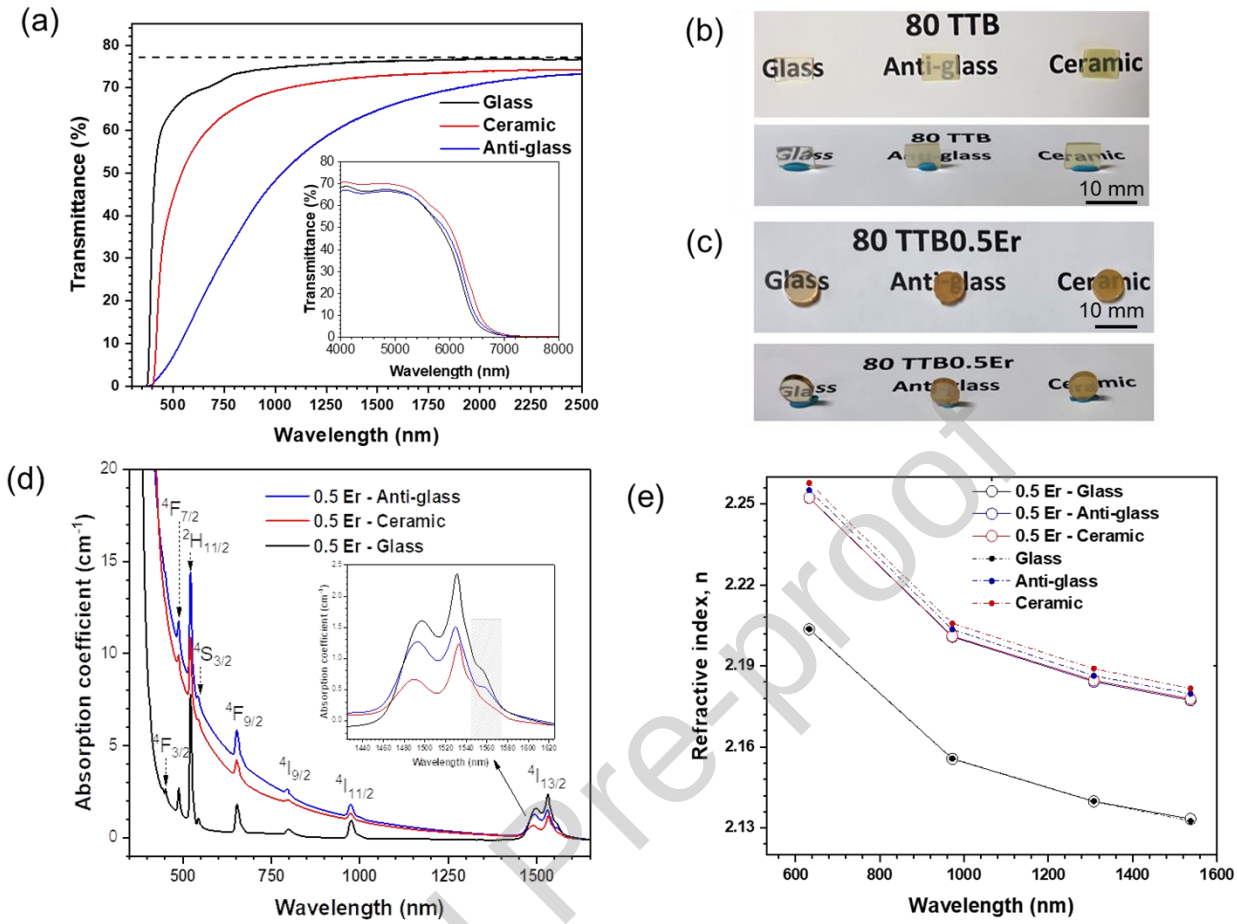

Figure 10. (a) Optical transmittance spectra of the 80TeO$_2$-10Ta$_2$O$_5$-10Bi$_2$O$_3$ parent glass, anti-glass and ceramic materials (thickness: 1 mm). The dotted black line corresponds to the theoretical maximum transmission of the glass calculated as 77% for an average refractive index of 2.132(5) determined at λ = 1537.7 nm). The inset shows the multiphonon absorption in the IR range. Photographs of the samples on the text and perpendicular of undoped (b) and Er^{3+} doped (c), (d) Absorption spectra of the Er^{3+}-doped samples. Figure inset shows the absorption band of the Er^{3+} corresponding to the $^4I_{15/2}\rightarrow{}^4I_{13/2}$ electronic transition, where different line shape absorption can be verified between these samples, (e) Refractive indices of the undoped and doped samples measured at 632.8, 972.4, 1308.2 and 1537.7 nm.

For undoped samples, the refractive index of the glass is lower compared to that of the anti-glass ($\Delta n = 0.032 \pm 0.004$) and ceramic ($\Delta n = 0.038 \pm 0.003$) at 632.8, 972.4, 1308.2 and 1537.7 nm. Such differences are mainly explained by the variation of the density evidenced between the glass sample and the anti-glass and ceramic samples (from 6.33 ± 0.02 g.cm^{-3} for the glass to 6.57 ± 0.02 g.cm^{-3} and 6.58 ± 0.02 g.cm^{-3} for the anti-glass and the ceramic samples respectively). In this framework, the Er^{3+}-doped samples also show a similar trend, though the refractive index values slightly decrease for the anti-glass as for the ceramic. Furthermore, the

values recorded for the anti-glass and the ceramic are approximately the same (Figure 10e), in agreement with the absorption/scattering coefficients displayed in Figure 10b. In this way, the refractive indices of Er^{3+}-doped anti-glass or ceramic samples are larger when compared with other kinds of tellurite glasses [35]–[37] and similar to refractive index values reported by Bertrand *et al.* for the TNB system (Nb replacing Ta) [18]. In this regard, such samples are also of interest as nonlinear optical materials.

The non-linearity of these materials was verified through the measurements of up-conversion (UC) emission spectra which were measured upon 980 nm excitation at room temperature in the range 400–750 nm as shown in Figure 11a. The spectra exhibit two emission bands (green and red ranges), for the Er^{3+}-doped glass and three emission bands (blue, green and red) for Er^{3+}-doped anti-glass and ceramic samples. The observed Er^{3+} emission in blue region is likely due to the higher non-linearity of these two latter samples compared to the Er^{3+}-doped glass sample, as mentioned above. Those emissions are observed due to a process of photon absorption by the $^4I_{11/2}$ excited level, known as excited state absorption (ESA). The $^4I_{11/2}$ energy level is thus populated by a 980 nm laser excitation. The green emission band corresponds to the most intense in comparison with the other bands in each sample. It is important to mention that a fraction of the Er^{3+} ions may relax to the $^4I_{13/2}$ state. But because of the relatively long lifetime of the $^4I_{11/2}$ state, the other fraction of the ions can absorb a second photon and reach the $^4F_{7/2}$ energy level. Subsequently, the electrons relax to the ground state $^4I_{15/2}$ by emitting the blue, green and red luminescence through ($\{^4F_{7/2}, {}^2H_{11/2}, {}^4S_{3/2}, {}^4F_{9/2}\} \rightarrow {}^4I_{15/2}$) transitions [34], [38]. Furthermore, for the glass sample, its intensity is about 2 and 4 times more intense than in the case of the anti-glass and the ceramic, respectively. In this context, focusing our attention on the green emission band, the doped glass samples have a high population fraction that rises to the upper levels, followed by the anti-glass sample and finally the ceramic. In addition, the $^2H_{11/2}$ and $^4S_{3/2}$ to $^4I_{15/2}$ transitions corresponding to green emission bands from Er^{3+} ion, are

hypersensitive transitions due to the selection rules |ΔS| = 1 and 0, |ΔL| ≤ 1 and 6, and |ΔJ| ≤ 2 and 6, respectively. Therefore, the emission spectra lineshape, both in up and down conversion luminescence as seen in Figure 11 are different in these three doped samples due to changes around Er^{3+} ions and even the nearest surroundings. Therefore, to determine the number of infrared photons involved in the population inversion process and ESA for each UC emission band, the relationship $I_{UC} \propto I^n$ was employed, where I_{UC} is the emission intensity which is proportional to the pump intensity I, and n must be an integer since it represents the photon numbers involved in the ESA process (number of IR photons absorbed per visible photon emitted) [39]. The power diode laser is in the [0.4 - 2.22 W] range. The fitted results are 2.0 ± 0.2 for the green emission band, *i.e.*, all samples show a two photon excitation process because they follow a quadratic power dependence in the low-power regime [40], [41].

On the other hand, when the samples are pumped at 377 nm, the down-conversion emission spectra are totally different from UC spectra (Figure 11b). The Er^{3+}-doped glass sample shows a traditional emission spectrum well-known in tellurite glasses [42]. Meanwhile, the other two samples show a broadband emission covering from 400 to 515 nm, which could be assigned to the existence of various localized energy states within the optical band gap of those two samples. In this region, the violet and blue emissions are thus strongly observed, centered at 410 ($^2H_{9/2} \rightarrow {}^4I_{15/2}$) and 445 ($^4F_{3/2} \rightarrow {}^4I_{15/2}$) nm in the anti-glass and ceramic samples doped with Er^{3+} ions but not in the glass sample. Such results could be due to a recombination of the electrons of the optical band of the samples with those of the Er^{3+} energy levels, which makes it possible for the electronic population in those energy levels to be higher and then improve the spontaneous emissions (see Figure 11b). Additionally, such emissions from the optical bands of the doped anti-glass and ceramic samples show different intensities but with a similar line shape. This behavior corresponds to the tails observed in the absorption spectra of both samples. On the other hand, their intensities emission in the green band change, and their line

shape also, which can be explained due to different population processes in the $^2H_{11/2}$ and $^4S_{3/2}$ energy levels, as well the different crystalline fields around the Er^{3+} ions.

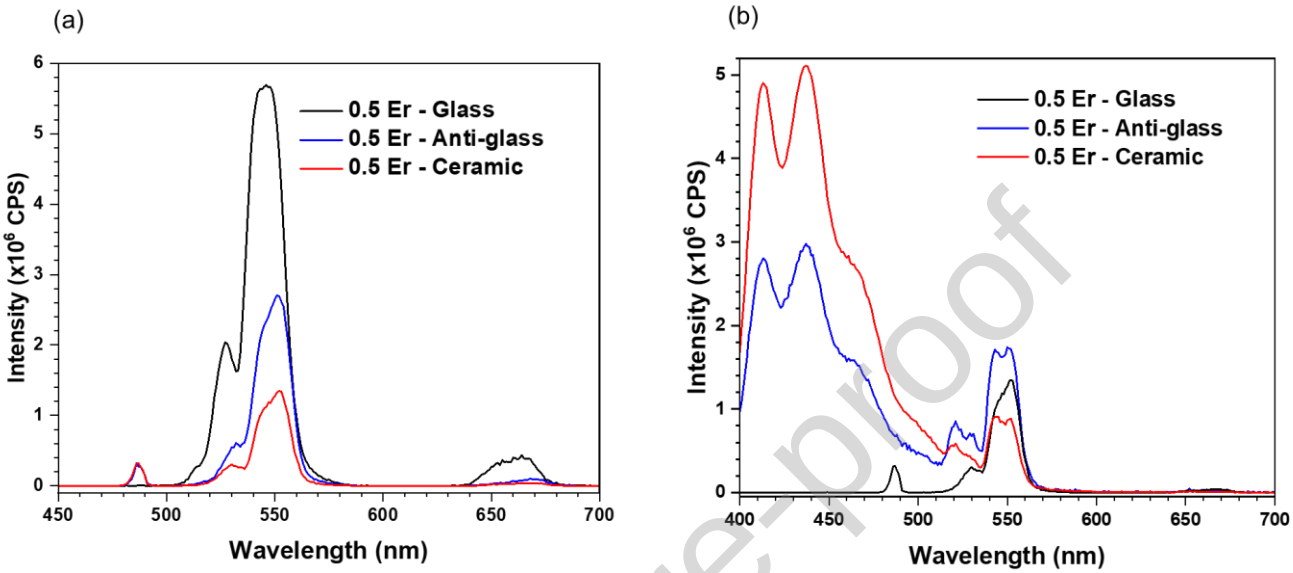

Figure 11. (a) Up-conversion luminescence of Er^{3+} under 980 nm laser excitation in the $80TeO_2$-$10Ta_2O_5$-$10Bi_2O_3$ glass, anti-glass and ceramic under 2.22W. (b) Down-conversion emission spectra of the samples excited with the Xenon source lamp centered at 377 nm.

Figure 12a shows the luminescence spectra of the $80TeO_2$-$10Ta_2O_5$-$10Bi_2O_3$ Er^{3+}-doped glass, anti-glass and ceramic when pumped at 980 nm. Such band corresponds to the $^4I_{13/2} \rightarrow {}^4I_{15/2}$ transition of the Er^{3+} ions. The anti-glass shows the highest emission intensity followed by the ceramic sample and the one with the least intensity is that of the glass sample for which the highest intensity peak is centered at 1532 ± 1 nm and the line shape is different. As mentioned above, an anti-glass has a long-range order like in crystals whose short-range order is highly disturbed hence a randomly distributed or missing anions, *i.e.*, it is opposite to a glass which has well defined short-range order. But, when Er^{3+} ions are introduced, the randomization sites decrease since the Er^{3+} causes covalent bonding, and thus a new short-range order could be obtained, *i.e.*, new sites around the Er^{3+} ions, which could increase the effect of the crystalline field thus modifying the bandwidth, the emission intensity and the transition probabilities of the Er^{3+} ions in the NIR region. Thus, in an anti-glass, the Er^{3+} ions find each other in different

sites in the network increasing the ions solubility and thus also the radiative transition probabilities of the different Stark sublevels, crystal field changes, resulting in an intensity emission improvement and an inhomogeneous broadening emission in comparison with a glass system. Also, such structural and microstructural changes (see Figures 7 to 9) provoke polarizability modifications around the Er^{3+} ions which could be responsible for such luminescence improvement. On the other hand, ceramic material exhibits many crystals which can improve the intensity emission in comparison with the glass and disordered anti-glass. However, such improvement in ceramic sample decreases the bandwidth of the emission spectrum of this sample in comparison with the glass. Therefore, we believe that the change in the crystalline field around the Er^{3+} ions during the crystallization process could be the main reason for improving the intensity emission and band emission in the anti-glass, then the ceramic and finally the glass (Figure 12b). As previously mentioned, the ceramic material exhibits a mixed occupancy of A (Bi and Ta) and B (Bi and Te) sites in the cubic structure as well as a superstructure at the nanometric scale that contributes to a high degree of disorder and which could explain these results. Even though numerous studies have reported tailoring the bandwidth emission of the Er^{3+} ions in tellurite glasses [34], [43], there is no value reported in the literature, according to our best knowledge, about Er^{3+}-doped tellurite anti-glass with 105 nm of bandwidth and intensities emission higher in comparison with the parent glass or corresponding ceramic.

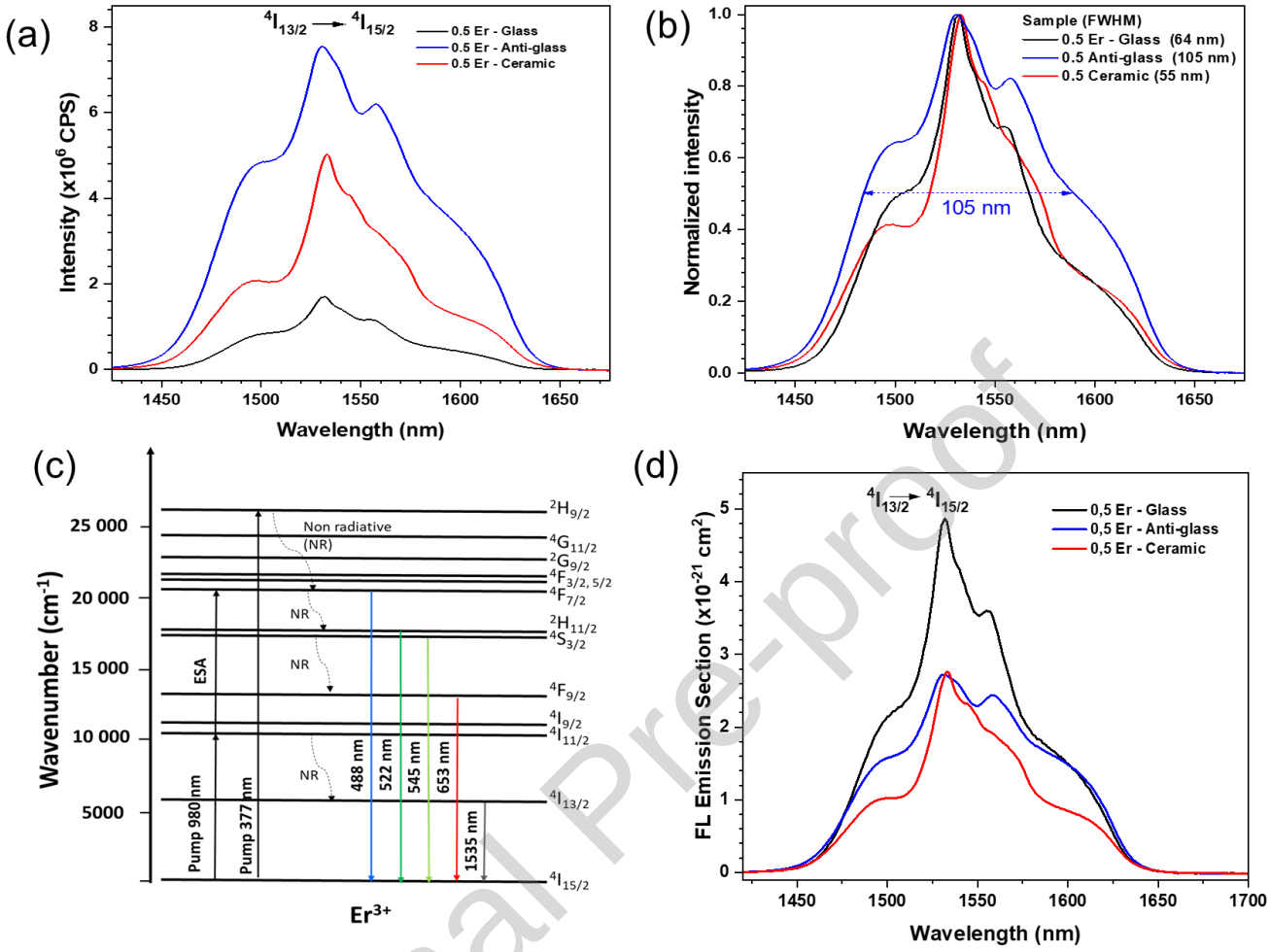

Figure 12. a) Down-conversion luminescence spectra of Er^{3+} in the $80TeO_2$-$10Ta_2O_5$-$10Bi_2O_3$ glass, anti-glass and ceramic under 2.22 W of laser excitation at 980 nm, b) Normalized luminescence spectra of the samples, c) Energy level diagram of Er^{3+} ion with proposed down- and up- conversion mechanism under 377 nm and 976 nm laser excitation. (d) Emission cross-sections of glasses by the Füchtbauer–Ladenburg theory at 980 nm laser excitation and 2.22 W laser power.

Down- and up- conversion processes under pumping at 377 nm and 980 nm are schematized in Figure 12c. In addition, the emission cross-sections are calculated using the Füchtbauer-Ladenburg (FL) theory, $\sigma_{ems}(\lambda) = \frac{\lambda^4}{8\pi c n^2 \tau} \frac{I(\lambda)}{\int I(\lambda)\, d\lambda}$, λ is the wavelength, I is the emission intensity (see Figure 12 a and b), c is the vacuum velocity of light, n is the refractive index and τ is the lifetime [44]. The emission cross-section spectra for the samples by the FL theory are shown in Figure 12d. It is important to mention that the maximum value of emission cross-

section for the glass, anti-glass and ceramic are 4.86/2.73/2.80×10^{-21} cm^2, respectively, which are different even though all samples are excited under the same conditions.

Another important parameter is the lifetime (centered at 1532 nm) of the $^4I_{13/2}$ excited state, when pumping at 980 nm. The latter varies from 4.5 ms (glass) to 5.6 ms (anti-glass) and up to 7.5 ms in the case of the ceramic (see Figure 13). Such monotonous increase is perfectly in agreement with the progressive structural ordering that was previously discussed in section 3.2. Here, the emission peak exhibits a single exponential decay. Lifetime values for the Er^{3+}-doped glass are similar to the literature [34], [43]. Lifetime is related to the total spontaneous emission probability, which is affected by the decrease or increase of the absorption cross section due to the disorder of the network, resulting in a lifetime decrease or increase. The oscillator strength for the electric dipole transition is given by [43]–[46]: $P_{i,.j} = \chi\left(\frac{8\pi^2 mv}{h}\right)\left|\left\langle i\left(=I^4_{13/2}\right)\middle|D^{(k)}_q\middle|j\left(=I^4_{15/2}\right)\right\rangle\right|^2$, where m is the electron mass, h is the Planck´s constant, ν is the frequency of the line transition, χ is a function of the refractive index of the medium in which the ion is embedded, $D^{(k)}_q = \sum_j r^{(k)}_j \sqrt{\frac{4\pi}{2k+1}} Y_{k,q}$ is the crystal field operator that depend of the environment around the Er^{3+} ions, $Y_{k,q}$ is the spherical harmonic function k (= 2, 4 or 6) is the degree and q is the order of $Y_{k,q}$, that is, the spatial distribution of the electric dipole. In addition, the radiative lifetime τ_i of an excited level i, the transition radiative probability, can be written as $\tau_i \propto \frac{1}{b_i u_i P_{i,j}}$. Here $u_i < 1$ since no all the electric dipole transition are radiative and b_i is the electronic population fraction that produces the transition between these two energy levels. Neglecting non-radiative decays produced by multi-phonons or other effects, the radiative lifetime will depend on the symmetry (order or disorder of the system), of the electric dipoles nature around the Er^{3+} ions, as well as the population distribution in each Stark sublevel. Therefore, here the symmetry of the system glass and other processes, *e.g.*, UC process, must be considered to describe the values of the lifetime reported here. In this manner,

the lower lifetime value in Er^{3+}-doped glass is in good agreement with the higher efficiency in the UC process (see Figure 11a), and hence, the population fraction in the $^4I_{13/2}$ decay quickly in comparison with the other two samples. The same reasoning can be finally applied to the anti-glass and ceramic samples: longer lifetimes together with a lower efficiency in the UC process.

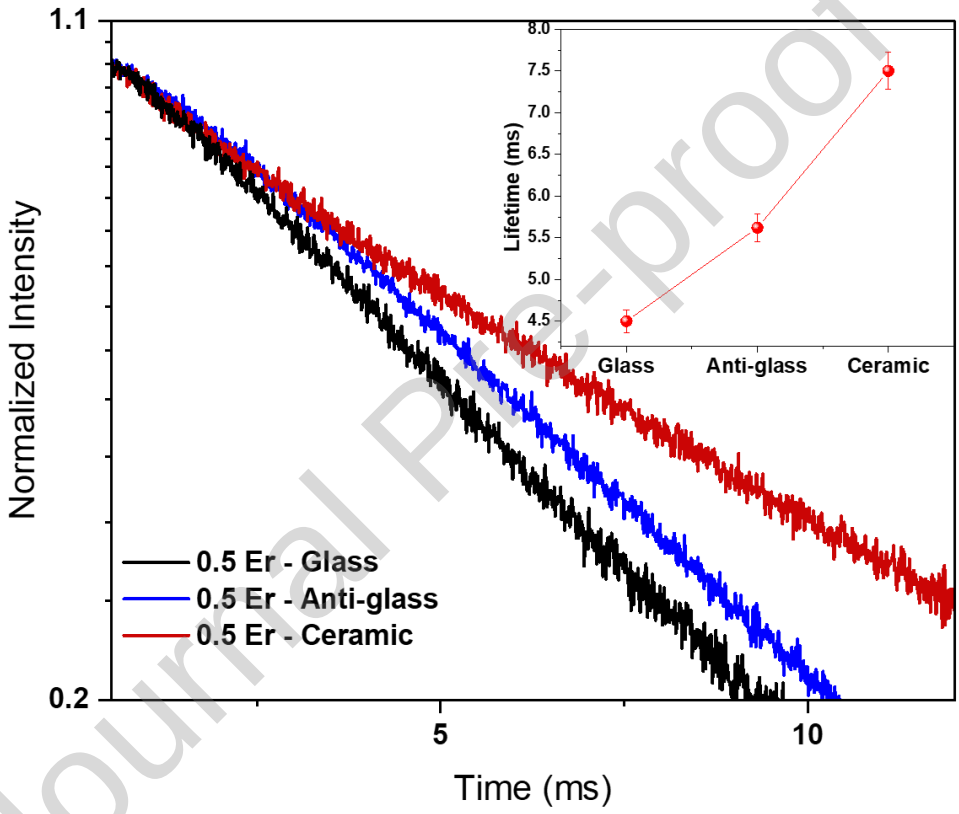

Figure 13. Experimental radiative decay record and the lifetime of the $^4I_{13/2}$ excited level as a function of the nature of the $80TeO_2$-$10Ta_2O_5$-$10Bi_2O_3$ samples (glass, anti-glass, ceramic). Pumping of the samples is carried out at 980 nm under 40 mW.

4- Conclusion

We reported on a detailed investigation of the elaboration, crystal structure, thermal and optical properties of the as-yet-unreported $Bi_{0.625}Ta_{0.625}Te_{2.75}O_8$ transparent ceramic. Bulk crystalline sample has been successfully synthesized from the crystallization of the $80TeO_2$-$10Ta_2O_5$-$10Bi_2O_3$ parent glass (80TTB) with the stabilization of an intermediate phase upon heating, a

disordered anti-glass. The congruent crystallization is at play in the case of the 80TTB parent glass composition.

X-ray diffraction and Rietveld refinement suggest that the crystal structure of $Bi_{0.625}Ta_{0.625}Te_3O_8$ is isostructural with the structure of $Bi_{0.8}Nb_{0.8}Te_{2.4}O_8$. Optical properties of these transparent ceramics are promising as a transmittance of 74%, close to the theoretical transmittance, in the near infrared range was recorded. The small grain size and complex microstructure evidenced in the transparent ceramic compound also favor good optical properties and garner some interest in this field. On a more general aspect, these results show that crystallizing amorphous phases can lead to the discovery of novel metastable phases with interesting functional properties.

The optical properties of Er^{3+}-doped 80TTB glass, anti-glass, and ceramic materials show that these materials' non-linearity impacts their up-conversion (UC) and emission spectra. Specifically, the anti-glass and ceramic samples displayed higher non-linearity than the glass samples. The introduction of Er^{3+} ions altered the crystalline field, which was found to significantly affect the emission intensity, bandwidth, and transition probabilities in the NIR region, particularly evident in the anti-glass samples. The symmetry of the system and the nature of electric dipoles around Er^{3+} ions also affected the radiative lifetime. These findings highlight the potential of these materials for use in photonics applications, especially towards the generation of ultrashort pulses.

Acknowledgements

The authors thank the Orléans Métropole for the financial support of the in situ high temperature XRD furnace. The project benefitted from the microscopy facilities of the Platform MACLE-CVL which was co-funded by the European Union and Center-Val de Loire Region (FEDER).

References

[1] R. A. H. El-Mallawany, *Tellurite Glasses Handbook*, 0 éd. CRC Press, 2016. doi: 10.1201/b11295.

[2] K. T. Vu, « Fabrication and characterisation of tellurite planar waveguides », p. 236.

[3] Victor. Lenher et Edward. Wolesensky, « A STUDY OF THE METALLIC TELLURITES. », *J. Am. Chem. Soc.*, vol. 35, nº 6, p. 718-733, juin 1913, doi: 10.1021/ja02195a007.

[4] Z. Xiao *et al.*, « Materials development and potential applications of transparent ceramics: A review », *Materials Science and Engineering: R: Reports*, vol. 139, p. 100518, janv. 2020, doi: 10.1016/j.mser.2019.100518.

[5] I. Milisavljevic, M. J. Pitcher, J. Li, S. Chenu, M. Allix, et Y. Wu, « Crystallization of glass materials into transparent optical ceramics », *International Materials Reviews*, p. 1-29, août 2022, doi: 10.1080/09506608.2022.2107372.

[6] M. Allix *et al.*, « Highly Transparent $BaAl_4O_7$ Polycrystalline Ceramic Obtained by Full Crystallization from Glass », *Adv. Mater.*, vol. 24, nº 41, p. 5570-5575, nov. 2012, doi: 10.1002/adma.201202282.

[7] S. Alahraché *et al.*, « Perfectly Transparent $Sr_3Al_2O_6$ Polycrystalline Ceramic Elaborated from Glass Crystallization », *Chem. Mater.*, vol. 25, nº 20, p. 4017-4024, oct. 2013, doi: 10.1021/cm401953d.

[8] K. Al Saghir *et al.*, « Transparency through Structural Disorder: A New Concept for Innovative Transparent Ceramics », *Chem. Mater.*, vol. 27, nº 2, p. 508-514, janv. 2015, doi: 10.1021/cm5037106.

[9] X. Ma *et al.*, « Pressureless glass crystallization of transparent yttrium aluminum garnet-based nanoceramics », *Nat Commun*, vol. 9, nº 1, p. 1175, déc. 2018, doi: 10.1038/s41467-018-03467-7.

[10] M. Dolhen *et al.*, « A comprehensive study of the glass/translucent anti-glass/transparent ceramic structural ordering in the Bi2O3Nb2O5–TeO2 system », *Acta Materialia*, vol. 189, p. 73-84, mai 2020, doi: 10.1016/j.actamat.2020.02.062.

[11] N. Berkaïne *et al.*, « Structure and Dielectric Properties of Tellurium Oxide-Based Materials », in *Ceramic Transactions Series*, K. M. Nair et S. Priya, Éd., Hoboken, NJ, USA: John Wiley & Sons, Inc., 2010, p. 63-74. doi: 10.1002/9780470930915.ch7.

[12] B. Jeansannetas *et al.*, « Glass Structure and Optical Nonlinearities in Thallium(I) Tellurium(IV) Oxide Glasses », *Journal of Solid State Chemistry*, vol. 146, nº 2, p. 329-335, sept. 1999, doi: 10.1006/jssc.1999.8355.

[13] O. Noguera et S. Suehara, « High nonlinear optical properties in TeO2-based glasses: A modifier's influence study from the localized hyperpolarizability approach », *Journal of Non-Crystalline Solids*, vol. 354, nº 2-9, p. 188-192, janv. 2008, doi: 10.1016/j.jnoncrysol.2007.08.089.

[14] Y. Wang, S. Dai, F. Chen, T. Xu, et Q. Nie, « Physical properties and optical band gap of new tellurite glasses within the TeO2–Nb2O5–Bi2O3 system », *Materials Chemistry and Physics*, vol. 113, nº 1, p. 407-411, janv. 2009, doi: 10.1016/j.matchemphys.2008.07.117.

[15] N. Gupta et A. Khanna, « Glass and anti-glass phase co-existence and structural transitions in bismuth tellurite and bismuth niobium tellurite systems », *Journal of Non-Crystalline Solids*, vol. 481, p. 594-603, févr. 2018, doi: 10.1016/j.jnoncrysol.2017.12.002.

[16] S. Blanchandin, P. Thomas, P. Marchet, J. C. Champarnaud-Mesjard, et B. Frit, « Equilibrium and non-equilibrium phase diagram within the TeO2-rich part of the TeO2-Nb2O5 system », *J. Mater. Chem.*, vol. 9, nº 8, p. 1785-1788, 1999, doi: 10.1039/a900788a.

[17] J. Lin *et al.*, « Crystallization of TeO2–Nb2O5 glasses and their network structural evolution », *Materials Science-Poland*, 2009.

[18] A. Bertrand *et al.*, « Scalable and Formable Tellurite-Based Transparent Ceramics for Near Infrared Applications », *Advanced Optical Materials*, vol. 4, nº 10, p. 1482-1486, oct. 2016, doi: 10.1002/adom.201600230.

[19] T. Komatsu, T. Honma, T. Tasheva, et V. Dimitrov, « Structural role of Nb2O5 in glass-forming ability, electronic polarizability and nanocrystallization in glasses: A review », *Journal of Non-Crystalline Solids*, vol. 581, p. 121414, avr. 2022, doi: 10.1016/j.jnoncrysol.2022.121414.

[20] G. Meunier, J. Galy, et P. Hagenmuller, « Sur une nouvelle série de composés de formule A0.5B0.5Te3O8 de type structural tite3o8 (A=Sc, Cr, Fe, Ga, Rh, In, Bi, et B=Nb, Ta) », *Acad. Sci.*, 1970.
[21] H. G. Burckhardt et M. Trömel, « Strontium-undecaoxotellurat, SrTe5O11, eine CaF2-Defektstruktur und ihre Beziehung zur Struktur einfacher Gläser », *Acta Crystallogr C Cryst Struct Commun*, vol. 39, nº 10, p. 1322-1323, oct. 1983, doi: 10.1107/S0108270183008380.
[22] M. Trömel, W. Hützler, et E. Münch, « Anti-glass phases and other lanthanide tellurates with fluorite-related structures », *Journal of the Less Common Metals*, vol. 110, nº 1-2, p. 421-424, août 1985, doi: 10.1016/0022-5088(85)90352-2.
[23] M. Trömel, E. Münch, G. Blasse, et G. J. Dirksen, « Formation and luminescence of lower symmetrical tellurite anti-glass phases », *Journal of Solid State Chemistry*, vol. 76, nº 2, p. 345-354, oct. 1988, doi: 10.1016/0022-4596(88)90229-0.
[24] O. Masson, P. Thomas, O. Durand, T. Hansen, J. C. Champarnaud, et D. Mercurio, « On the structure of the disordered Bi2Te4O11 phase », *Journal of Solid State Chemistry*, vol. 177, nº 6, p. 2168-2176, juin 2004, doi: 10.1016/j.jssc.2004.03.010.
[25] A. Bertrand *et al.*, « New Transparent Glass-Ceramics Based on the Crystallization of "Anti-glass" Spherulites in the Bi_2O_3–Nb_2O_5–TeO_2 System », *Crystal Growth & Design*, vol. 15, nº 10, p. 5086-5096, oct. 2015, doi: 10.1021/acs.cgd.5b01048.
[26] J.-P. Laval *et al.*, « Highly transparent fluorotellurite glass-ceramics: structural investigations and luminescence properties », p. 8.
[27] R. Piotrowski *et al.*, « Transparent glass-ceramics in the TeO_2–InF_3 system », *Int J of Appl Glass Sci*, vol. 13, nº 4, p. 568-575, oct. 2022, doi: 10.1111/ijag.16581.
[28] I. Yakine, M. Naji, A. Chagraoui, A. Moussaoui, et A. Tairi, « Synthesis, structure refinement and vibrational spectroscopy studies of the Bi1−xTa1−xTe2xO4 ($0 \leq x \leq 0.2$) solid solution with stibiotantalite type structure », *Materials Chemistry and Physics*, vol. 135, nº 2-3, p. 241-248, août 2012, doi: 10.1016/j.matchemphys.2012.05.038.
[29] I. Yakine, A. Chagraoui, A. Moussaoui, et A. Tairi, « Synthesis and characterization of new amorphous and crystalline phases in Bi2O3-Ta2O5-TeO2 system », p. 10, 2012.
[30] J. Rodríguez-Carvajal, « Recent Developments of the program FULLPROF. », *Commission on Powder Diffraction Newsletter*, 2001.
[31] N. Gupta, A. Khanna, Hirdesh, A.-C. Dippel, et O. Gutowski, « Structure of bismuth tellurite and bismuth niobium tellurite glasses and $Bi_2Te_4O_{11}$ anti-glass by high energy X-ray diffraction », *RSC Adv.*, vol. 10, nº 22, p. 13237-13251, 2020, doi: 10.1039/D0RA01422B.
[32] T. Sekiya, N. Mochida, et A. Soejima, « Raman spectra of binary tellurite glasses containing tri- or tetra-valent cations », *Journal of Non-Crystalline Solids*, vol. 191, nº 1-2, p. 115-123, nov. 1995, doi: 10.1016/0022-3093(95)00290-1.
[33] C. Joseph, P. Bourson, et M. D. Fontana, « Amorphous to crystalline transformation in Ta2O5 studied by Raman spectroscopy: Amorphous to crystalline transformation in Ta2O5 studied by Raman spectroscopy », *J. Raman Spectrosc.*, vol. 43, nº 8, p. 1146-1150, août 2012, doi: 10.1002/jrs.3142.
[34] V. A. G. Rivera et D. Manzani, Éd., *Technological Advances in Tellurite Glasses: Properties, Processing, and Applications*, vol. 254. in Springer Series in Materials Science, vol. 254. Cham: Springer International Publishing, 2017. doi: 10.1007/978-3-319-53038-3.
[35] G. Lakshminarayana *et al.*, « Concentration dependent structural, thermal, and optical features of Pr 3+ -doped multicomponent tellurite glasses », *Journal of Alloys and Compounds*, vol. 686, p. 769-784, nov. 2016, doi: 10.1016/j.jallcom.2016.06.069.
[36] G. Lozano C., J. Chacaliaza-Ricaldi, J. L. Clabel H., Y. Messaddeq, V. A. G. Rivera, et E. Marega, « Improving emission performance and bandwidth broadening of the Er3+-doped tellurite – tungsten glasses at 1.5 μm via Pr3+ ions », *Journal of Luminescence*, vol. 260, p. 119853, août 2023, doi: 10.1016/j.jlumin.2023.119853.
[37] I. C. Pinto, R. F. Falci, V. A. G. Rivera, T. Guérineau, S. LaRochelle, et Y. Messaddeq, « Novel insights on energy transfer processes in [Ce4+/Ce3+]-Er3+-doped tellurite glass », *Ceramics International*, vol. 49, nº 4, p. 6613-6619, févr. 2023, doi: 10.1016/j.ceramint.2022.10.156.

[38] R. Debnath, A. Ghosh, et S. Balaji, « Synthesis and luminescence properties of an (Er2Te4O11) nanocrystals dispersed highly efficient upconverting lead free tellurite glass », *Chemical Physics Letters*, vol. 474, nº 4-6, p. 331-335, juin 2009, doi: 10.1016/j.cplett.2009.05.001.
[39] V. A. G. Rivera, F. A. Ferri, L. A. O. Nunes, et E. Marega, « White light generation via up-conversion and blue tone in Er3+/Tm3+/Yb3+-doped zinc-tellurite glasses », *Optical Materials*, vol. 67, p. 25-31, mai 2017, doi: 10.1016/j.optmat.2017.03.028.
[40] A. M. Pires, O. A. Serra, S. Heer, et H. U. Güdel, « Low-temperature upconversion spectroscopy of nanosized Y_2O_3:Er,Yb phosphor », *Journal of Applied Physics*, vol. 98, nº 6, p. 063529, sept. 2005, doi: 10.1063/1.2058195.
[41] G. L. C., V. A. G. Rivera, Y. Messaddeq, et E. M. Jr., « Thermometry and optical study of Er3+-Yb3+ doped tellurite glasses as a suitable candidate for optical fibre », *Journal of Alloys and Compounds*, vol. 948, p. 169777, juill. 2023, doi: 10.1016/j.jallcom.2023.169777.
[42] A. Lemiere, B. Bondzior, I. Aromäki, et L. Petit, « Study of visible, NIR, and MIR spectroscopic properties of Er^{3+} -doped tellurite glasses and glass–ceramics », *J Am Ceram Soc.*, vol. 105, nº 12, p. 7186-7195, déc. 2022, doi: 10.1111/jace.18649.
[43] S. J. Ikhmayies, Éd., *Advances in Glass Research*. in Advances in Material Research and Technology. Cham: Springer International Publishing, 2023. doi: 10.1007/978-3-031-20266-7.
[44] H. C. Çamiçi, T. Guérineau, V. A. G. Rivera, R. F. Falci, S. LaRochelle, et Y. Messaddeq, « The role of tungsten oxide in Er3+-doped bismuth-germanate glasses for optical amplification in L-band », *Scientific Reports*, vol. 13, nº 1, p. 8835, mai 2023, doi: 10.1038/s41598-023-35995-8.
[45] B. R. Judd, « Optical Absorption Intensities of Rare-Earth Ions », *Phys. Rev.*, vol. 127, nº 3, p. 750-761, août 1962, doi: 10.1103/PhysRev.127.750.
[46] M. P. Hehlen, M. G. Brik, et K. W. Krämer, « 50th anniversary of the Judd–Ofelt theory: An experimentalist's view of the formalism and its application », *Journal of Luminescence*, vol. 136, p. 221-239, avr. 2013, doi: 10.1016/j.jlumin.2012.10.035.
[47] B. R. Judd, « Optical Absorption Intensities of Rare-Earth Ions », *Phys. Rev.*, vol. 127, nº 3, p. 750-761, août 1962, doi: 10.1103/PhysRev.127.750.
[48] B. M. Walsh, « Judd-Ofelt theory: principles and practices », in *Advances in Spectroscopy for Lasers and Sensing*, B. Di Bartolo et O. Forte, Éd., Dordrecht: Springer Netherlands, 2006, p. 403-433. doi: 10.1007/1-4020-4789-4_21.

Declaration of Competing Interest

☒ The authors declare that they have no known competing financial interests or personal relationships that could have appeared to influence the work reported in this paper.